RESEARCH PAPER

Fully nonlinear modeling of radiated waves generated by floating flared structures

Bin-Zhen Zhou · De-Zhi Ning · Bin Teng · Ming Zhao

Abstract The nonlinear radiated waves generated by a structure in forced motion, are simulated numerically based on the potential theory. A fully nonlinear numerical model is developed by using a higher-order boundary element method (HOBEM). In this model, the instantaneous body position and the transient free surface are updated at each time step. A Lagrangian technique is employed as the time marching scheme on the free surface. The mesh regridding and interpolation methods are adopted to deal with the possible numerical instability. Several auxiliary functions are proposed to calculate the wave loads indirectly, instead of directly predicting the temporal derivative of the velocity potential. Numerical experiments are carried out to simulate the heave motions of a submerged sphere in infinite water depth, the heave and pitch motions of a truncated flared cylinder in finite depth. The results are verified against the published

B.-Z. Zhou
College of Ship Building Engineering,
Harbin Engineering University, 150001 Harbin, China

B.-Z. Zhou · D.-Z. Ning · B. Teng (✉)
State Kay Laboratory of Coastal and Offshore Engineering,
Dalian University of Technology, 116023 Dalian, China
e-mail: bteng@dlut.edu.cn

M. Zhao
School of Computing, Engineering and Mathematics,
University of Western Sydney, Penrith,
2751 NSW, Australia

numerical results to ensure the effectiveness of the proposed model. Moreover, a series of higher harmonic waves and force components are obtained by the Fourier transformation to investigate the nonlinear effect of oscillation frequency. The difference among fully nonlinear, body-nonlinear and linear results is analyzed. It is found that the nonlinearity due to free surface and body surface has significant influences on the numerical results of the radiated waves and forces.

1 Introduction

In recent years, although accurate and efficient numerical models develop rather fast, it is still a challenge to simulate strong nonlinear wave–structure interaction. For many years, the perturbation expansion in terms of wave steepness and the Taylor approximation of boundary conditions on the mean water and body surfaces have been widely used to derive the linear, second-order and even much higher-order theories [1–4]. Such methods are valid only when the wave amplitude and the body motion amplitude are small relative to the wavelength and the representative dimension of the body, respectively. Most of early studies on the waves generated by moving bodies were based on either linear or higher-order perturbation analyses. For example, Goren [5] used the second-order theory to simulate the waves generated by the oscillations of a truncated cylinder in the frequency domain. Isaacson & Ng [6] and Teng et al. [7] carried out second-order time-domain simulations of similar problems.

When the body motion amplitude relative to its dimension is not small, the nonlinearity of the body motion can not be ignored. Since updating the body surface is not as complex as updating the free surface, the so-called body-nonlinear method was developed, where linear (or higher-order) free surface and nonlinear body-boundary conditions are applied. The body-nonlinear method has been applied

to frequency-domain [8, 9] and time-domain [10, 11] for simulating wave radiation problems. Ferrant [12] used a coupled time and frequency approach to simulate a submerged sphere undergoing large amplitude motions. Qiu & Peng [13] employed the time-domain Green function to simulate the waves generated by a submerged sphere and a truncated vertical cylinder under prescribed motions.

If the motion of the body and the wave surface are strongly nonlinear, a fully nonlinear model should be used to ensure accuracy. The fully nonlinear time-domain method, initially introduced by Longuet-Higgins and Cokelet [14], has been developed and applied to many water wave problems in parallel with the rapid growth of the numerical technique and the computer capacity. The major difficulties associated with the fully nonlinear method lie in the modeling of the time-varying free surface, the treatment of the intersection between the body and the water surface and the tremendous computational cost etc. Additionally, the numerical instability is another problem to be solved. Recent applications of fully nonlinear models for simulating the nonlinear wave diffraction and radiation problems include the finite element models (FEM) [15–20] and the HOBEM models [21–28]. Among these applications, Hu et al. [17] and Wang et al. [20] calculated the fully nonlinear radiated wave field using the finite element method (FEM), and Bai and Eatock Taylor [23] using the HOBEM.

The applications above-mentioned are mostly dealing with submerged bodies or cylindrical floating structures. with no variation of the cross section in the vertical direction. In fact, the nonlinear effect will become more pronounced for non-wall-sided structures, such as flared structures. As stated in Ref. [20], the presence of the flare makes the simulation more complicated. Firstly, the projection of the waterline on a horizontal plane varied with time because of the flare. This requires. mesh regeneration to be more flexible and be able to efficiently deal with arbitrary shapes. The flare could also cause a rapid variation in pressure and velocity. This will require finer mesh and small time step if the same accuracy is desired as that for wall-sided structures. Because of these reasons, there has been far less work on wave radiation by 3D non-wall-sided structures. based on the fully nonlinear model.

The aim of this study is to develop a fully nonlinear numerical model to investigate the wave radiation by three-dimensional submerged structures and surface-piercing structures with flare undergoing forced motions. The model is developed by using a time-domain HOBEM based on the potential theory. One advantage of the HOBEM is that the remeshing is much easier in comparison with the FEM. Another advantage is that it is easier to calculate the velocities at grid points, and to determine the intersection be-

tween the body and the water surfaces. A Lagrangian technique is used as the time marching scheme on the free surface, and the mesh regridding and interpolation techniques are adopted to mitigate the possible numerical instability. Hydrodynamic forces are calculated based on some auxiliary functions instead of directly calculating the temporal derivative of the potential. Numerical experiments are carried out to simulate a submerged sphere in heave motion and a truncated flared structure undergoing heave and pitch motions. The corresponding hydrodynamic forces on the structures and radiation waves are investigated comprehensively. A series of higher-harmonic forces and wave elevation components are derived by Fourier transformation and compared with the body-nonlinear results. By comparing the fully nonlinear results with the numerical results of both linear and body-nonlinear methods, the importance of the nonlinearities from the free surface and the body surface is discussed extensively. The nonlinear features of waves and hydrodynamic forces have been captured in larger wave steepness (i.e., large oscillation amplitude or high frequency). The comparison indicates that the fully- and the body-nonlinear results are in good agreement with each other at smaller wave steepness, and differ from each other at larger wave steepness. With the increase of wave steepness, the nonlinearity is expected to become more prominent.

2 Mathematical formulations

2.1 Boundary value problem and numerical schemes

To describe a forced moving body in an open sea with water depth d, two right-handed Cartesian coordinate systems are defined in Fig. 1. One is a space-fixed coordinate system $oxyz$ with the oxy plane on the mean free surface and with the z-axis being positive upwards. The other is a body-fixed coordinate system $o'x'y'z'$ with its origin o' placed at the center of mass of the body. When the body is at its equilibrium position, these two sets of coordinate systems are parallel. In Fig. 1, S_F, S_B, and S_D represent the free surface, the body surface and the bottom surface, respectively. The centre of mass is located initially at $\boldsymbol{X}_{c0}$ in the space-fixed coordinate system, and at $\boldsymbol{X}_c$ ($= \boldsymbol{X}_{c0} + \boldsymbol{\zeta}$) subsequently. Here $\boldsymbol{\zeta} = (\zeta_1, \zeta_2, \zeta_3)$ is introduced to denote the translational displacements of surge, sway and heave, and the Euler angles $\boldsymbol{\theta} = (\alpha, \beta, \gamma)$ is defined to illustrate the angles of roll, pitch and yaw, which are rotations about x', y', and z', respectively. The relationships between the two systems can be written as

$$\begin{pmatrix} x \\ y \\ z \end{pmatrix} = \begin{pmatrix} x_{c0} \\ y_{c0} \\ z_{c0} \end{pmatrix} + \begin{pmatrix} \zeta_1 \\ \zeta_2 \\ \zeta_3 \end{pmatrix} + \boldsymbol{C} \begin{pmatrix} x' \\ y' \\ z' \end{pmatrix}, \tag{1}$$

where [29]

$$\boldsymbol{C} = \begin{bmatrix} \cos\beta\cos\gamma & -\cos\beta\sin\gamma & \sin\beta \\ \sin\alpha\sin\beta\cos\gamma + \cos\alpha\sin\gamma & -\sin\alpha\sin\beta\sin\gamma + \cos\alpha\cos\gamma & -\sin\alpha\cos\beta \\ -\cos\alpha\sin\beta\cos\gamma + \sin\alpha\sin\gamma & \cos\alpha\sin\beta\sin\gamma + \sin\alpha\cos\gamma & \cos\alpha\cos\beta \end{bmatrix}. \tag{2}$$
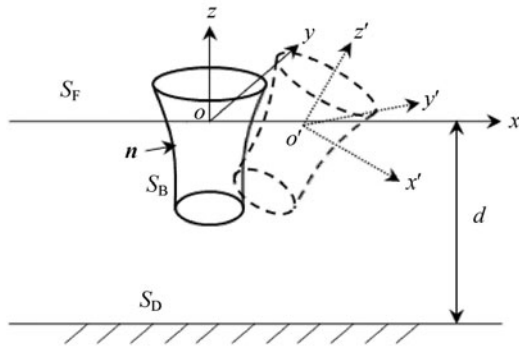
Fig. 1 Sketch of coordinate system and computational domain

Assuming that the fluid is ideal and incompressible, and flow is irrotational, the velocity potential ϕ (x, y, z, t) can be introduced, which satisfies the Laplace equation in the fluid domain R

$$\nabla^2 \phi = 0. \tag{3}$$

On the instantaneous free water surface S_F, the fully nonlinear kinematic and dynamic boundary conditions in the Lagrangian expression can be written as [23]

$$\left. \begin{aligned} \frac{\mathrm{D}\boldsymbol{X}}{\mathrm{D}t} &= \nabla\phi, \\ \frac{\mathrm{D}\phi}{\mathrm{D}t} &= \frac{1}{2}\nabla\phi \cdot \nabla\phi - g\eta, \end{aligned} \right\} \quad \text{on } S_F, \tag{4}$$

where g is the acceleration due to gravity, $\boldsymbol{X} = (x, y, z)$ denotes the position vector of a free surface particle, η is the elevation of water surface above its mean level, $\frac{\mathrm{D}}{\mathrm{D}t} = \frac{\partial}{\partial t} + \boldsymbol{u} \cdot \nabla$ is the full derivative with $\boldsymbol{u}$ being the velocity of the fluid particle. In the linear wave theory, the linear free-surface conditions are

$$\left. \begin{aligned} \frac{\partial \eta}{\partial t} &= \frac{\partial \phi}{\partial z}, \\ \frac{\partial \phi}{\partial t} &= -g\eta, \end{aligned} \right\} \quad \text{on } z = 0. \tag{5}$$

The kinematic condition on the instantaneous wetted body surface S_B is

$$\frac{\partial \phi}{\partial t} = \boldsymbol{V} \cdot \boldsymbol{n}, \tag{6}$$

where $\boldsymbol{V}$ is the velocity of the body surface, $\boldsymbol{n}$ is the normal unit vector of the surface pointing out of the fluid domain, as shown in Fig. 1. The body surface velocity can be expanded as

$$\boldsymbol{V} = \boldsymbol{U} + \boldsymbol{\Omega} \times \boldsymbol{r}_b, \tag{7}$$

where $\boldsymbol{r}_b = \boldsymbol{X}'$ is the position vector in the body-fixed coordinate system, $\boldsymbol{U}$ is the translational velocity of the reference point on the body at $\boldsymbol{r}_b = 0$, and $\boldsymbol{\Omega}$ in the equation is the rotational velocity of the body about x', y', z', respectively.

For the linear model, the linear free-surface conditions in Eq. (5) and the body-boundary condition in Eq. (6) are sat-isfied on the mean position of water surface and body surface. For the body-nonlinear model, the linear free-surface conditions Eq. (5) are satisfied on the mean water surface, and the body-boundary condition Eq. (6) on the instantaneous wetted body surface.

In order to avoid the abrupt initial condition during the initial time steps, a cosine ramp function R_m is used to modulate the above body-surface condition. R_m is taken as

$$R_m = \begin{cases} \frac{1}{2}\left[1 - \cos\left(\frac{\pi t}{T_m}\right)\right], & \text{if } t \leqslant T_m, \\ 1, & \text{if } t > T_m, \end{cases} \tag{8}$$

where T_m is chosen here as twice the excitation period or $2T$.

An artificial damping layer is applied on the outer annulus of the circular domain to absorb the scattered wave energy. In the present study, both ϕ- and η-type damping terms are added to the free surface conditions in Eq. (4) [23]. Finally, as the body starts to oscillate from rest in still water, the initial velocity potential and wave elevation can be set to zero.

2.2 Higher-order boundary element method

By applying Green's second identity in the fluid domain R, the above mentioned boundary value problem can be converted into the following boundary integral equation

$$\alpha(\boldsymbol{p})\phi(\boldsymbol{p}) = \iint_S \left(\phi(\boldsymbol{q})\frac{\partial \boldsymbol{G}(\boldsymbol{p}, \boldsymbol{q})}{\partial n} - \boldsymbol{G}(\boldsymbol{p}, \boldsymbol{q})\frac{\partial \phi(\boldsymbol{q})}{\partial n}\right)\mathrm{d}s, \tag{9}$$

where $\boldsymbol{p} = (x_0, y_0, z_0)$ and $\boldsymbol{q} = (x, y, z)$ are source and field points, respectively, $\alpha(\boldsymbol{p})$ is the ratio of the solid angle to 4π. S stands for all the boundaries and $\boldsymbol{G}$ is the simple Green function.

For cases in which the computational domain is symmetric about the x–z plane and the seabed is horizontal, the simple Rankine source and its image with respect to the symmetry plane ($y = 0$) and the seabed ($z = -d$) can be chosen as the Green function. Thus, only half of the computational domain is considered, and the seabed is excluded. Similarly, for cases in which the computational domain is symmetric about both the x–z and the y–z plane, and the seabed is flat, the simple Rankine source and its image with respect to the symmetry planes ($y = 0$ and $x = 0$) and the seabed can be chosen as the Green function. The integration needs to be evaluated over a quarter of the computational boundaries only, and the seabed is excluded. Under these conditions, the Green function can be written as Eq. (10). For the present computation, M equals eight for the heave motion, while four for the pitch motion.

$$\boldsymbol{G}(\boldsymbol{p}, \boldsymbol{q}) = -\frac{1}{4\pi}\sum_{i=1}^{M}\frac{1}{R_i}, \tag{10}$$

where

$$R_1 = \sqrt{(x-x_0)^2 + (y-y_0)^2 + (z-z_0)^2},$$
$$R_2 = \sqrt{(x-x_0)^2 + (y+y_0)^2 + (z-z_0)^2},$$
$$R_3 = \sqrt{(x-x_0)^2 + (y-y_0)^2 + (z+z_0+2d)^2},$$
$$R_4 = \sqrt{(x-x_0)^2 + (y+y_0)^2 + (z+z_0+2d)^2},$$
$$R_5 = \sqrt{(x+x_0)^2 + (y-y_0)^2 + (z-z_0)^2},$$
$$R_6 = \sqrt{(x+x_0)^2 + (y+y_0)^2 + (z-z_0)^2},$$
$$R_7 = \sqrt{(x+x_0)^2 + (y-y_0)^2 + (z+z_0+2d)^2},$$
$$R_8 = \sqrt{(x+x_0)^2 + (y+y_0)^2 + (z+z_0+2d)^2}. \tag{11}$$

The higher-order boundary element method is used to solve the above boundary value problem at each time step. The boundary surface is discretized by the quadratic isoparametric elements. After introducing shape functions $h(\xi, \varsigma)$ [30] in each surface element, one can write the position coordinate, the velocity potential and its derivatives within an element in terms of nodal values as follows

$$\boldsymbol{X}(\xi, \varsigma) = \sum_{k=1}^{K} h_k(\xi, \varsigma)\boldsymbol{X}_k,$$

$$\phi(\xi, \varsigma) = \sum_{k=1}^{K} h_k(\xi, \varsigma)\phi_k, \tag{12}$$

$$\frac{\partial \phi}{\partial n} = \sum_{k=1}^{K} h_k(\xi, \varsigma)\left(\frac{\partial \phi}{\partial n}\right)_k,$$

where (ξ, ς) represents the local intrinsic coordinates; $\boldsymbol{X}_k$, ϕ_k, $(\partial\phi/\partial n)_k$ and h_k are the coordinates, potentials, normal derivatives of the potential and the shape functions corresponding to the k-th node in the local system; K is the total number of nodes in the element (eight for quadrilateral and six for triangle).

By substituting Eq. (12) into Eq. (9), the integral equation is formulated in the following form

$$\alpha(\boldsymbol{p})\phi(\boldsymbol{p}) = \sum_{n=1}^{N}\sum_{m=1}^{M} \frac{\partial \boldsymbol{G}(\boldsymbol{p}, \boldsymbol{q}_m)}{\partial n}\left(\sum_{k=1}^{K} h_k(\xi, \varsigma)\phi_k\right)$$
$$\times \omega_m |J_m(\xi, \varsigma)| - \sum_{n=1}^{N}\sum_{m=1}^{M} \boldsymbol{G}(\boldsymbol{p}, \boldsymbol{q}_m)$$
$$\times \left(\sum_{k=1}^{K} h_k(\xi, \varsigma)\frac{\partial \phi_k}{\partial n}\right)\omega_m |J_m(\xi, \varsigma)|, \tag{13}$$

where M is the number of samping points used in the standard Gauss–Legendre method to evaluate numerically the integration over each element, ω_m is the integral weight at the m-th sampling point, $J_m(\xi, \varsigma)$ represents the Jacobian transformation from the global to the local intrinsic coordinates, and N is the total number of elements. $\boldsymbol{p}$ is an arbitrary point on the free surface and other discretized boundaries.

The final matrix equation is obtained by imposing Eq. (13) at all the nodal points

$$\boldsymbol{Ax} = \boldsymbol{B}, \tag{14}$$

in which $\boldsymbol{x}$ includes the unknown nodal normal velocities on the free surface and nodal potentials on the solid surfaces, $\boldsymbol{A}$ is the influence coefficient matrix and $\boldsymbol{B}$ is a column obtained from the known terms of Eq. (13).

2.3 Hydrodynamic forces

Hydrodynamic forces on the body $\boldsymbol{F} = \{f_1, f_3, f_3\}$ and moments $\boldsymbol{N} = \{f_4, f_5, f_6\}$ can be obtained by integrating the pressure over the wetted body surface

$$f_i = \iint_{S_B} P n_i \mathrm{d}s$$
$$= -\rho \iint_{S_B} \left(\frac{\partial \phi}{\partial t} + \frac{1}{2}|\nabla\phi|^2 + g\eta\right) n_i \mathrm{d}s,$$
$$i = 1, 2, \cdots, 6, \tag{15}$$

where ρ is the fluid density, $\boldsymbol{n} = (n_1, n_2, n_3)$, and $\boldsymbol{r}_b \times \boldsymbol{n} = (n_4, n_5, n_6)$. The calculation of the last two terms in Eq. (15) is straightforward. However, it is non-trivial to evaluate ϕ_t. This term can be calculated using the backward finite difference method in the perturbation expansion technique, which requires calculating the same nodes at two moments. However, for the fully nonlinear problem, integration should be carried out on the wetted body surface and the nodes moving with the time. So the backward finite difference method is inaccurate and may even be prone to instability, particularly for a floating body. To overcome this difficulty, we use the method developed by Wu [31, 32], which has also been successfully used by Kashiwagi [33] and Bai & Eatock Taylor [24–26]. In this approach, some auxiliary functions ψ_i ($i = 1, 2, \cdots, 6$) are introduced, instead of direct computation of ϕ_t (details can be found in Ref. [30]). These functions satisfy the Laplace equation in the fluid and the corresponding boundary conditions. Finally, the hydrodynamic forces can be given by the following expression

$$f_i = -\rho \iint_{S_B} \psi_i(\dot{\boldsymbol{U}} + \dot{\boldsymbol{\Omega}} \times \boldsymbol{r}_b) \cdot \boldsymbol{n}\mathrm{d}s$$
$$+ \rho \iint_{S_B} \{\nabla\psi_i[(\boldsymbol{U} + \boldsymbol{\Omega} \times \boldsymbol{r}_b) \cdot \boldsymbol{n}]\cdot$$
$$[\nabla\phi - (\boldsymbol{U} + \boldsymbol{\Omega} \times \boldsymbol{r}_b)] + \psi_i(\boldsymbol{\Omega} \times \boldsymbol{U}) \cdot \boldsymbol{n}\}\mathrm{d}s$$
$$- \rho \iint_{S_B + S_F} \left(gz + \frac{1}{2}\nabla\phi \cdot \nabla\phi\right)\frac{\partial \psi_i}{\partial n}\mathrm{d}s, \tag{16}$$

where the dot over $\boldsymbol{U}$ and $\boldsymbol{\Omega}$ indicates the derivatives with respect to time.

3 Mesh regridding and interpolation

As the Lagrangian method is used, the saw-tooth appearance will develop in the numerically computed wave profile after a sufficiently long period of time due to particle nodes moving horizontally and vertically. Remeshing on the free surface is implemented to remove the numerical instability due to

the saw-tooth appearance. For moving boundary problems, we need to move the nodes horizontally prior to the vertical interpolation in order to maintain a good aspect ratio of the elements. To implement this process, the mesh on the instantaneous free surface is projected onto the horizontal plane. Then it is divided into the inner subdomain S_{in} and the outer subdomain S_{out}, as illustrated in Fig. 2. These two subdomains are separated by circle A (the solid line in Fig. 2) at the initial time, and the inner subdomain moves together with the body in the horizontal plane (indicated by the dot line in Fig. 2), in order to guarantee the elements around the body to be smooth. Meanwhile, the radius of the circle remains unchanged. The mesh distribution in the inner subdomain is generated by the conventional orthogonal grid. The meshing in the outer subdomain is carried out based on the elliptic partial differential equations. Cubic B-Spline function is employed to create new sets of equally spaced (in arc length) grid points on the intersection line, and the horizontal coordinates of the new nodes are then obtained. Once the new nodes on the boundary line of the free surface are known, the original mesh method is used to obtain other new nodes on the free surface.
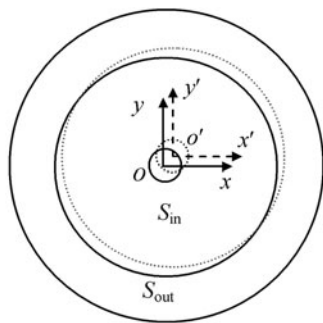

Fig. 2 Sketch of free surface domain division

When the horizontal coordinates of new nodes are obtained, interpolation can be employed to calculate the wave elevation as well as the potential of new nodes. For a node $P(x_i, y_i)$ in new mesh, we first find node Q in the old mesh which is closest to P. The elements in old mesh surrounding node Q are numbered as $m = 1, 2, \cdots, N$. We then seek a solution for (ξ, ς) in element m by the following equation [34]

$$x_i - \sum_{k=1}^{K} h_k(\xi, \varsigma) x_k^m = 0,$$

$$y_i - \sum_{k=1}^{K} h_k(\xi, \varsigma) y_k^m = 0,$$

$$(17)$$

based on the Newton–Raphson iteration method, where (x_k^m, y_k^m) is the nodal horizontal coordinates in element m. If the solution satisfies

$$|\xi| \leqslant 1, \quad |\varsigma| \leqslant 1, \tag{18}$$

P must lie inside this element. The vertical coordinate and

potential at P can be subsequently obtained by using the shape function within this element.

The total velocity of fluid particle $\boldsymbol{u}$ on the waterlines can be expressed as three components (u_x, u_y, u_z) in the x, y and z directions, that is (ϕ_x, ϕ_y, ϕ_z), and it can also be denoted by $(u_{\tau_1}, u_{\tau_2}, u_n)$ in two tangential directions $\boldsymbol{\tau}_1, \boldsymbol{\tau}_2$ and one normal direction $\boldsymbol{n}$ at the same point on the body surface. $\boldsymbol{\tau}_1$ and $\boldsymbol{\tau}_2$ can be any two vectors perpendicular to $\boldsymbol{n}$. For certainty, $\boldsymbol{\tau}_1$ is chosen to be $\boldsymbol{\tau}_1 = \boldsymbol{n} \times \boldsymbol{e}_y$ (or $\boldsymbol{\tau}_1 = \boldsymbol{n} \times \boldsymbol{e}_x$ if $\boldsymbol{n} \times \boldsymbol{e}_y = 0$), where $\boldsymbol{e}_x$ and $\boldsymbol{e}_y$ are unit vectors along the $+x$ and $+y$ axes in the space coordinate system, i.e., $\boldsymbol{e}_x = (1, 0, 0)$ and $\boldsymbol{e}_y = (0, 1, 0)$, while $\boldsymbol{\tau}_2$ is determined by $\boldsymbol{\tau}_2 = \dfrac{\boldsymbol{\tau}_1 \times \boldsymbol{n}}{|\boldsymbol{\tau}_1 \times \boldsymbol{n}|}$. Three velocity components (u_x, u_y, u_z) can be obtained by the above mentioned method, and the velocity components $(u_{\tau_1}, u_{\tau_2}, u_n)$ in directions $\boldsymbol{\tau}_1, \boldsymbol{\tau}_2$ and $\boldsymbol{n}$ are estimated by the following equations

$$u_{\tau_1} = (u_x, u_y, u_z) \cdot \boldsymbol{\tau}_1,$$

$$u_{\tau_2} = (u_x, u_y, u_z) \cdot \boldsymbol{\tau}_2, \tag{19}$$

$$u_n = (u_x, u_y, u_z) \cdot \boldsymbol{n}.$$

In general, the velocity normal component u_n is not equal to the normal velocity of the body $\boldsymbol{V} \cdot \boldsymbol{n}$ in Eq. (6), which will lead to the nodes on the waterlines separate from the body surface. In order to ensure the nodes on the waterlines are always on the body surface, the fluid velocity component u_n is replaced by the normal velocity of the body V_n, i.e., $\boldsymbol{V} \cdot \boldsymbol{n}$, then the new velocity of the fluid $\boldsymbol{u}'$ can be derived as

$$\begin{bmatrix} u_x' \\ u_y' \\ u_z' \end{bmatrix} = \begin{bmatrix} u_{\tau_1} \\ u_{\tau_2} \\ V_n \end{bmatrix} \begin{bmatrix} \tau_{1x} & \tau_{1y} & \tau_{1z} \\ \tau_{2x} & \tau_{2y} & \tau_{2z} \\ n_x & n_y & n_z \end{bmatrix}. \tag{20}$$

Then the new spatial derivative of the potential ϕ can be corrected by the new velocity of the fluid $\boldsymbol{u}'$. By substituting the new spatial derivative of the potential into Eq. (4), the material derivatives $D\boldsymbol{X}/Dt$, and $D\phi/Dt$ can be obtained and then the free surface particle is updated by the revised velocity, which will ensure the fluid particle on the intersections moves together with the body and remains on the body surface. When steep waves are simulated, the smoothing based on the scheme of Longuett-Higgins and Cokelet [14] is applied on the waterline.

Takes a vertical cylinder in surge motion as an example, the process of mesh regridding on the free surface is presented in Fig. 3. Figure 3a is the initial mesh on the free surface. After the cylinder moves in the horizontal direction, the mesh is deformed, as shown in Fig. 3b. The mesh near the body is uneven and the orthogonality deteriorates. For the problem of wave–structure interactions, the change of wave field near bodies is significant. Poor quality grids will induce instability of numerical calculations. Therefore, mesh regridding is needed to ensure high quality grids. Figure 3c presents the new mesh on the free surface according

to the above mesh regridding method, in which the dividing line is changed from the dotted line to the heavy solid line. It can be seen from Fig. 3c that the uniformity and orthogonality of grids near the cylinder are improved, while they deteriorate far away from the cylinder. Because the variation of wave field is relatively slow far away from the body, the impact on the whole calculation is small. Consequently, mesh regridding by the above method can make the mesh near the body always maintain high quality.

After mesh regeneration on the free surface, the process of mesh regridding on the body surface is presented in Fig. 4, which takes a cylinder with flare in heave motion for example. Figure 4a shows the initial mesh on the surface of the body with an initial draft $B/R = 1.5$. After the body moves in the vertical direction, the wetted body surface has been changed. Figures 4b and 4c show the instantaneous mesh on the wetted body surface when the displacement of the body is $\zeta_3 = 0.5R$ and $-0.5R$, respectively. It is noticeable that the numbers of grids remain unchanged, but the size of them varies. Moreover, compared with the initial grids shown in Fig. 4a, the grids in Fig. 4b are compressed, while they are stretched in Fig. 4c.
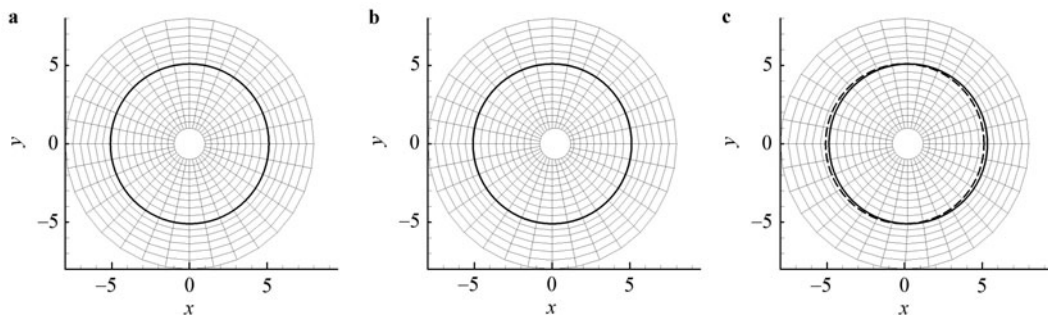
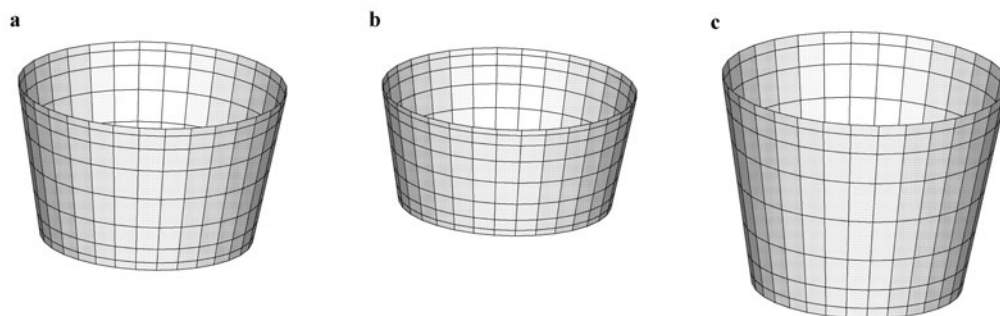**Fig. 3** Sketch of mesh regridding on the free surface. **a** Initial mesh; **b** Deformated mesh; **c** Regenerated mesh

Fig. 4 Sketch of mesh regridding on the body surface. **a** $\zeta_3 = 0$; **b** $\zeta_3 = 0.5R$; **c** $\zeta_3 = -0.5R$

4 Numerical results and discussions

In this section, numerical experiments are carried out for a submerged sphere in heave motion and a truncated cylinder with flare undergoing heave and pitch motions. The displacement of the body is governed by $\zeta_i = a_i \sin(\omega t)$, where ω is the oscillation frequency and a_i represents the motion amplitude of the body motion. Also throughout the study, t defines the real time and $T = 2\pi/\omega$ defines the period of the oscillatory motion.

4.1 A fully submerged sphere in heave motion

Firstly, the problem of a submerged sphere undergoing forced sinusoidal heave motion in infinite water depth is considered, as shown in Fig. 5. The distance between the sphere centre and the mean water surface is $Z_0/R = 2$, with R being the radius of the sphere. For different cases, mesh dependency study has been carried out, and it was found that

further increase in mesh density makes little difference on the numerical results. As an example, the distributions of the mesh on the free surface and the sphere surface for $kR = 2.0$ are shown in Fig. 6. There are totally 675 elements on the
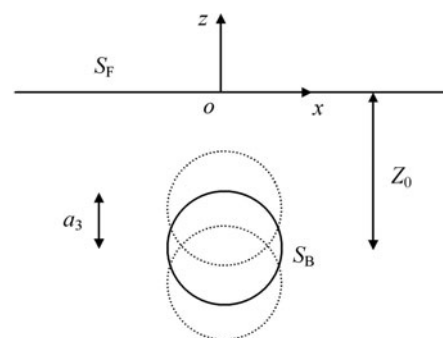

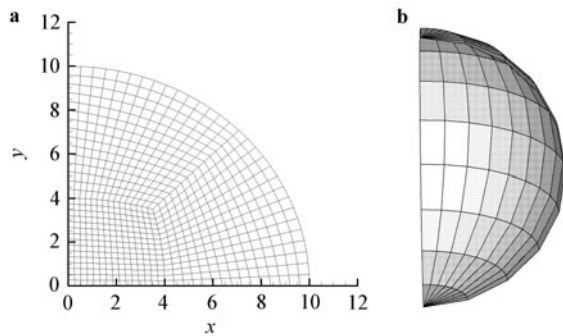**Fig. 5** Sketch of a submerged sphere in heave motion in infinite water depth

Fig. 6 Illustration of the initial mesh generation on the free surface and the sphere surface at $kR = 2.0$. **a** On the free surface; **b** On the sphere surface

water surface and 49 elements on the sphere surface. The computational time step is set to be $\Delta t = T/60$ for all the following cases. To absorb scattering waves, the outer annulus radius of the damping zone is set to be 1.5λ for $kR > 1.25$ and λ for other wave numbers. In the following discussion, the linear results, the body-nonlinear results and the fully nonlinear results are used to stand for the numerical results from the linear model, the body-nonlinear model and the fully nonlinear model, respectively.

In order to testify the accuracy of the present numerical method, the hydrodynamic forces acting on the submerged sphere are compared with the published results of Ferrant [12]. Ferrant carried out numerical simulations with nonlinear body condition and linear free surface conditions. From Fig. 7, it can be seen that the body-nonlinear results are in good agreement with the numerical results of Ferrant [12], which are also based on the body-nonlinear theory. The results based on the fully- and the body-nonlinear models agree well with each other in Fig. 7a, where the oscillation frequency is small, while the difference between them is much significant at higher oscillation frequency, as illustrated in Fig. 7b. It seems that, the difference arises from the nonlinear effect of the free surface boundary conditions. Moreover, the nonlinearity of the free surface becomes more pronounced at higher oscillation frequency.

The cases of $kR = 2.0$ and three values of motion amplitude of $a_3/R = 0.1, 0.3$, and 0.5 are computed by the fully nonlinear model. Figure 8 shows the time histories of wave elevations at $(3R, 0)$ and the vertical forces on the sphere. The figure reveals that the changes in wave elevations are quite noticeable especially at higher oscillation amplitude. The wave crests and the wave troughs become smaller with the increase of motion amplitude. However, no strong nonlinearity is noticed in vertical forces as the motion amplitude increases, which is because the pressure below the free surface is relatively small and the wetted body surface is constant for the submerged body.
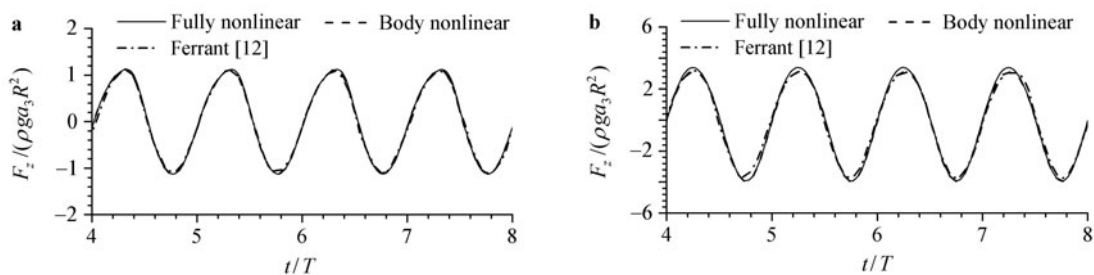

Fig. 7 Vertical forces on the submerged sphere in heave motion at $a_3/R = 0.5$. **a** $kR = 0.5$; **b** $kR = 2.0$
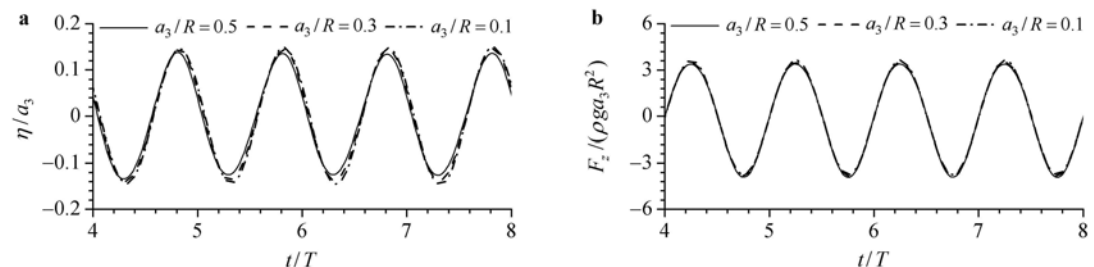

Fig. 8 Wave elevations at $(3R, 0)$ and vertical forces on the submerged sphere in heave motion at $kR = 2.0$. **a** Wave elevations at $(3R, 0)$; **b** Vertical forces

In order to investigate the effect of wave number on the results, wave elevations at $(3R, 0)$ and vertical forces are calculated for oscillation amplitude of $a_3/R = 0.5$ and different wave numbers. The time histories of wave elevations at $(3R, 0)$ and two wave numbers of $kR = 0.5, 2.0$ are given in Fig. 9. The corresponding vertical forces for $kR = 0.5$ and 2.0 have been illustrated in Fig. 7. From Figs. 7a and 9a, it can be seen that the influence of nonlinearity on wave ele-

vations is much stronger than that on vertical forces at lower frequency. At $kR = 0.5$, the second-harmonic component of wave elevations, which can not be detected in the linear results, is significant in the fully nonlinear results. Figure 9a demonstrates the limitation of the linear model on predicting the wave elevations. The body-nonlinear results in Fig. 9a are closer to the fully nonlinear results compared with the linear results. However, the body-nonlinear results are still different from the fully nonlinear results, indicating the significance of the free surface nonlinearity.

The calculated wave elevations at $(3R, 0)$ and the vertical forces in four steady-state wave periods are decomposed into harmonic components by the Fourier transformation. Figure 10 shows the 1st- and 2nd-harmonic wave elevations versus the wave number kR. The 1st-harmonic wave elevation ($\eta^{(1)}/a_3$) increases with increasing kR until $kR = 1.25$, beyond which $\eta^{(1)}/a_3$ starts decreasing with increasing kR. It can be seen from Fig. 10a that the agreement among the fully nonlinear, body-nonlinear and linear methods is good

only at small kR. With increasing wave number, the difference among the three methods becomes more prominent. In addition, it is clear that the 1st-harmonic wave elevation reaches a maximum at $kR = 1.25$. The difference in the 2nd-harmonic wave elevation between the fully- and the body-nonlinear models may be ascribed to the existence of some power exchanges between different wave frequencies. So the contribution from some high or higher frequencies can not be reflected by the linear solutions and the body-nonlinear results. The above analysis also shows that the fully nonlinear method is the only correct choice in strong nonlinear wave circumstance. Figure 11 presents the 1st- and 2nd-harmonic vertical forces versus the wave number kR. The difference in the 1st-harmonic force among the three methods is small. The difference between the fully- and the body-nonlinear 2nd-harmonic force increases with increasing kR as $kR > 1.25$. From the above comparison, it can be seen that the difference between the fully- and the body-nonlinear results becomes significant for strong nonlinear waves.
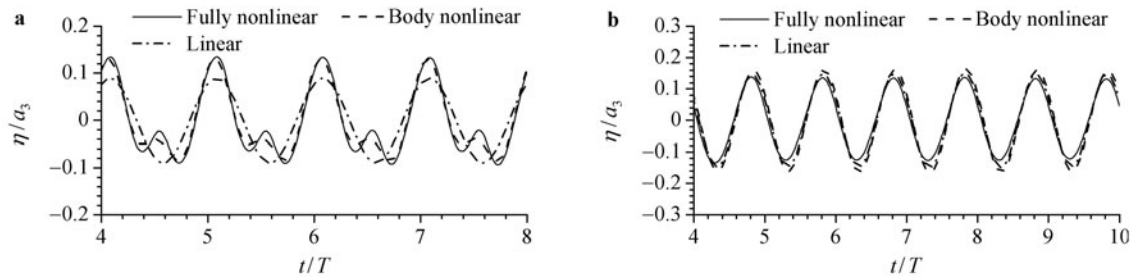

Fig. 9 Wave elevations at $(3R, 0)$ for the submerged sphere in heave motion at $a_3/R = 0.5$. **a** $kR = 0.5$; **b** $kR = 2.0$
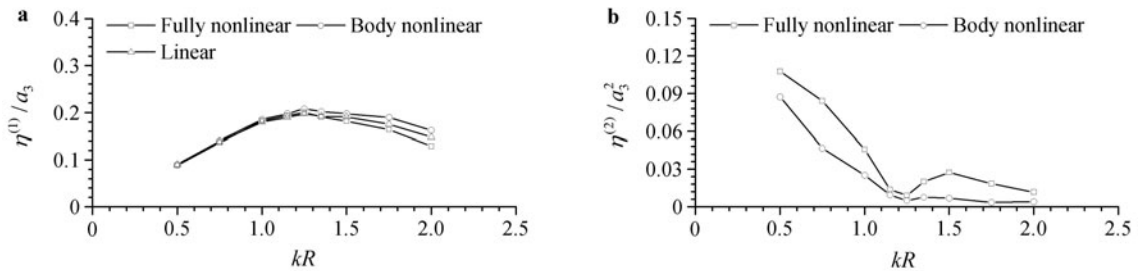

Fig. 10 The 1st- and 2nd-harmonic wave elevations at $(3R, 0)$ at $a_3/R = 0.5$ versus kR. **a** 1st-harmonic; **b** 2nd-harmonic
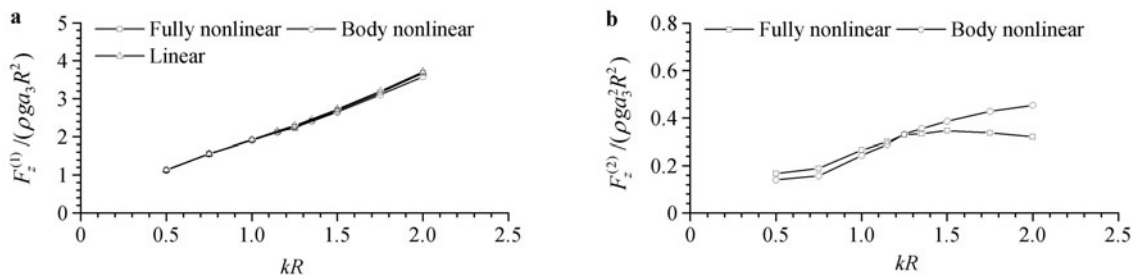

Fig. 11 The 1st- and 2nd-harmonic vertical forces on the submerged sphere at $a_3/R = 0.5$ versus kR. **a** 1st-harmonic; **b** 2nd-harmonic

4.2 A truncated cylinder with flare in heave motion

In this and the following subsection, the wave radiation by a truncated cylinder with flare shown in Fig. 12 in various forced motions is investigated. The symbol θ is defined as the angle between the flare and the horizontal plane, and r_d denotes the radius of the bottom circular surface of the cylinder. In all the following simulations of the truncated flared cylinder, the water depth is set to be $d/r_d = 3$ and the initial draught of the cylinder is $B/r_d = 1.5$. The flare angle is $\theta = 80°$ unless otherwise specified.

A cylinder with $\theta = 80°$ in vertical oscillation is first considered. The distribution of the mesh on the free surface and the body surface for $kr_d = 2.0$ is shown in Fig. 13. There are totally 864 elements on the water surface and 384 elements on the body surface. For the heave cases, a half of elements are used in Fig. 13, because the computational domain is symmetric about both the x–z and the y–z plane. All the numerical results of the present study used time step $\Delta t = T/60$. Mesh dependency and temporal-convergence studies for all examples have been carried out, and it was found that further increasing in mesh density and decreasing in computational time step makes little difference on the numerical results. To absorb scattering waves, the outer annulus radius of the damping zone is set to be 1.5λ for $kr_d > 1.25$ and λ for other wave numbers.
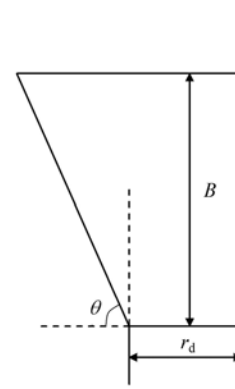

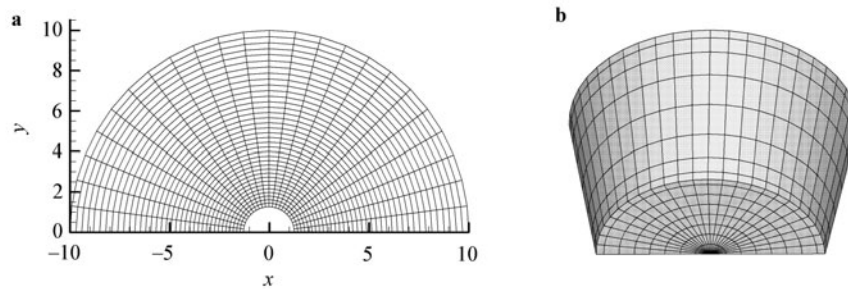**Fig. 12** Definition of a truncated cylinder with flare

Fig. 13 Illustration of the initial mesh generation on the free surface and the flared cylinder surface at $kr_d = 2.0$. **a** On the free surface; **b** On the flared cylinder surface

Figure 14 presents the comparison of wave elevations at $(2r_d, 0)$ and vertical forces with the fully nonlinear results of Wang et al. [20] at $kr_d = 2.0$, $a_3/r_d = 0.3$. It can be seen from Fig. 14 that the present fully nonlinear results are in reasonably good agreement with the results of Wang et al. [20]. The body-nonlinear results are slightly different from the fully nonlinear results because the free surface is treated linearly. Figure 15 gives the time histories of wave elevations at $(2r_d, 0)$ and the vertical forces on the cylinder for excitation amplitude of $a_3/r_d = 0.15$, 0.3, 0.6 at $kr_d = 2.0$.

The figure clearly reveals that no strong nonlinearity is noticed in the wave elevations, except the wave crests tend to be sharper and deeper than the troughs which appear with the increase of heave amplitude. However, the changes in the vertical forces are quite noticeable especially at larger amplitude, as high harmonics occur, which clearly indicate the presence of high nonlinearity. Such strong nonlinearity is mainly due to the variation of wetted surface of the cylinder during heave motion.
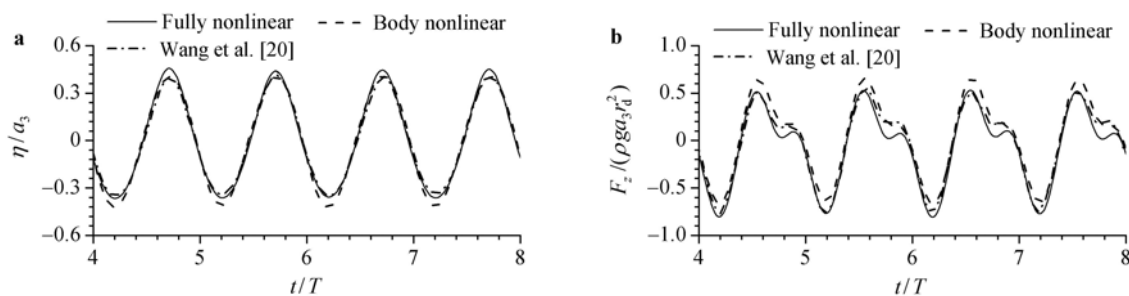

Fig. 14 Comparison of wave elevations and vertical forces on the cylinder with $\theta = 80°$ in heave motion at $kr_d = 2.0$, $a_3/r_d = 0.3$. **a** Waves elevations at $(2r_d, 0)$; **b** Vertical forces
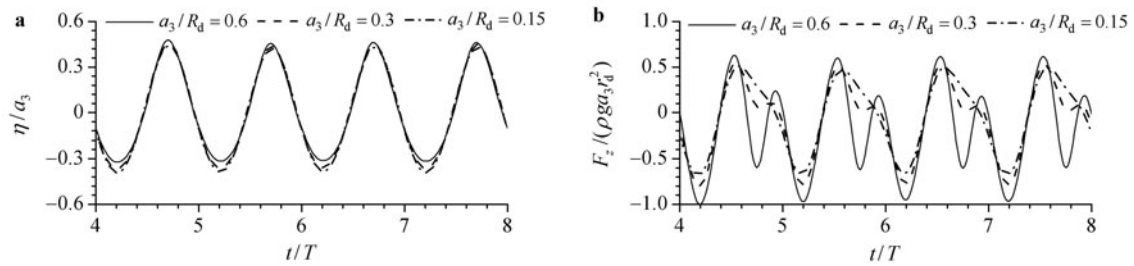
Fig. 15 Wave elevations and vertical forces on the cylinder with $\theta = 80°$ in heave motion at $kr_d = 2.0$. **a** Waves elevations at $(2r_d, 0)$; **b** Vertical forces

Further calculations are then carried out for a variety of wave numbers. Numerical results are analyzed by Fourier analysis to evaluate the 1st- and 2nd-harmonic components of wave elevations and the vertical forces. Figures 16 and 17 present respectively the 1st- and 2nd-harmonic wave elevation and the vertical force components versus the wave number at $a_3/r_d = 0.3$. The body-nonlinear and linear results are also presented for comparison. It can be seen from Figs. 16 and 17b that, the difference in the 1st- and 2nd- harmonic wave elevations and the 2nd-harmonic vertical forces between the two models increases with the increase of wave number, while the difference in the 1st-harmonic vertical forces is weak. The comparison indicates that the fully- and the body-nonlinear results are in good agreement with each other at smaller wave steepness, and differ from each other at larger wave steepness, indicating the importance of free-surface nonlinearity. With the increase of wave numbers, the nonlinearity is expected to become more remarkable. In the body-nonlinear model, the body boundary conditions are applied at the actual time depending body surface whereas the free surface conditions are linearized. In contrast, the fully nonlinear model seems to capture the higher-harmonics quite well. From the above discussion, the calculated hydrodynamic forces induced by heave motion of a body from different models could be different significantly, especially when the body is in large-amplitude vertical motion.
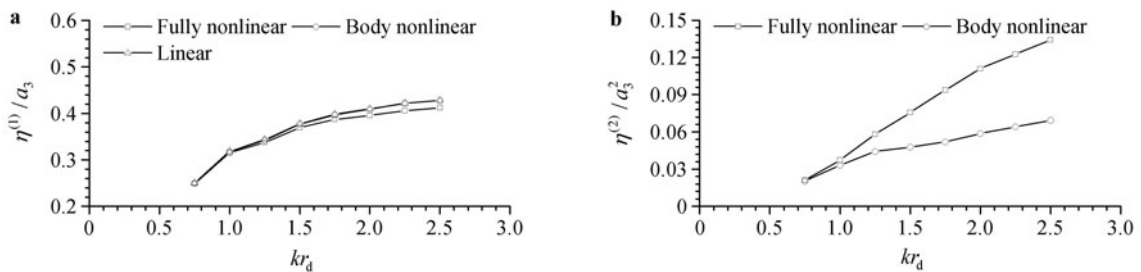

Fig. 16 Comparison of the 1st- and 2nd-harmonic wave elevations at $(2r_d, 0)$ for the cylinder with $\theta = 80°$ in heave motion at $a_3/r_d = 0.3$. **a** 1st-harmonic; **b** 2nd-harmonic

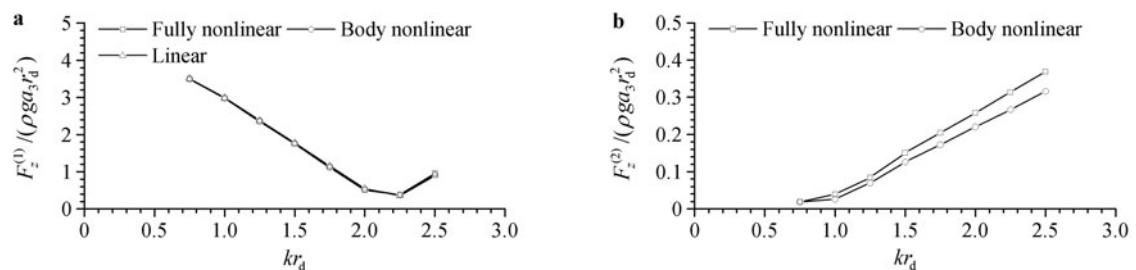**Fig. 17** Comparison of the 1st- and 2nd-harmonic vertical forces on the cylinder with $\theta = 80°$ in heave motion at $a_3/r_d = 0.3$. **a** 1st-harmonic; **b** 2nd-harmonic

Comparison is also made for three different structures. with $\theta = 85°$, $80°$, $75°$ based on the fully nonlinear method. The case of $kr_d = 2.0$ and $a_3/r_d = 0.3$ is calculated, and the results are presented in Fig. 18. The wave elevations are given at $(2r_d, 0)$, as in previous cases. As expected, the cylinder with greater flare in vertical motion creates larger radiated waves, which is consistent with the result of Wang et al. [20]. Moreover, the peaks of the vertical force on the

cylinder with greatest flare are visibly the largest. This is partly because the sides of the cylinder with flare also provide a contribution to the vertical force, and the level projection area of the side surface is larger for the cylinder with greater flare. The other reason is that $\theta = 75°$ corresponds

to a larger water plane area. Relative to the diameter of the water plane, the draught of the cylinder is smaller in the case of $\theta = 75°$. The change at the bottom of the cylinder has, therefore, a larger effect on the results.
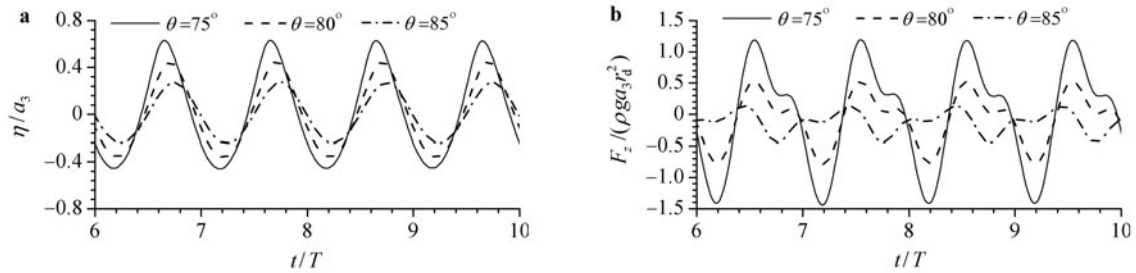

Fig. 18 Influence of flare on wave elevations and vertical forces on the body in heave motion at $kr_d = 2.0$ and $a_3/r_d = 0.3$ based on the fully nonlinear method. **a** Wave elevations at $(2r_d, 0)$; **b** Vertical forces

4.3 A truncated cylinder with flare in pitch motion

Finally, a truncated cylinder with flare undergoing pitch motion about its mass center $(0, 0, 0)$ is investigated. The prediction of the intersection line between the free surface and the rotating body surface, and mesh regeneration on the free surface and the body surface become more complicated. Therefore, there are rarely fully nonlinear results of the rotation problem in publications. Figure 19 presents the time histories of wave elevation at $(2r_d, 0)$ and the hydrodynamic forces and moment on the cylinder with $\theta = 80°$ for three different pitch angles at $kr_d = 2.0$. From the figure, it can be seen that with increasing pitch amplitude, the wave crest becomes larger, and the wave trough is found to be smaller. Moreover, it can be observed that the increase of motion amplitude does not produce any noticeable change on the hori-

zontal forces and the moment about the y-axis. In addition, the vertical force is smaller in comparison with the horizontal force, but it increases rapidly with the increase of oscillation amplitude. The vertical force appears to oscillate at double frequency of the body motion, which is consistent with the conclusion of Bai and Eatock Taylor [23] and Wang et al. [20]. On the basis of the linear theory, for the surge or pitch motion of a body which is symmetric about the y-axis, the wave field is anti-symmetric about the y-axis. The vertical force must be zero. However, the second order wave field is not anti-symmetry anymore, and will generate the second-order force.

Then the impact of oscillation frequency on the 1st- and 2nd-harmonic wave elevation components and the harmonic forces and moment is given in Figs. 20 and 21. For the analysis presented here, the motion amplitude of the body is kept
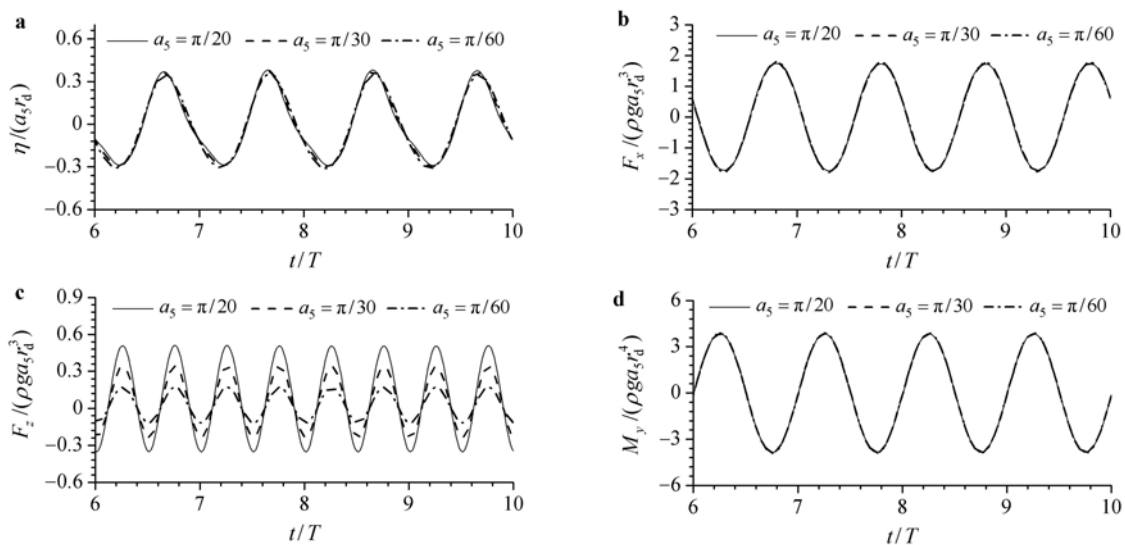

Fig. 19 Wave elevations, hydrodynamic forces and moment on the cylinder in pitch motion at $kr_d = 2.0$. **a** Wave elevations at $(2r_d, 0)$; **b** Horizontal forces; **c** Vertical forces; **d** Moment about the y-axis
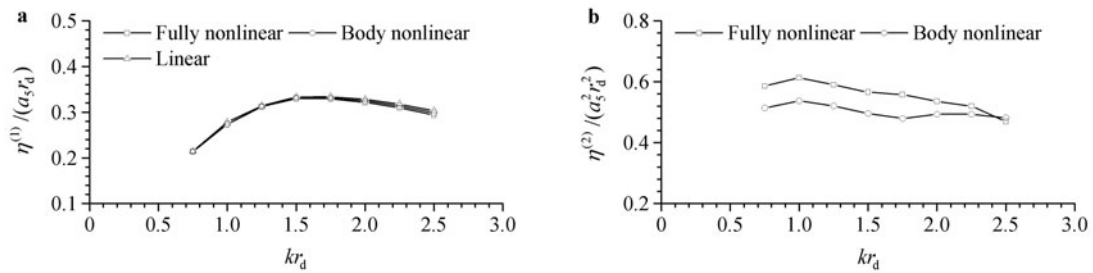
Fig. 20 Comparison of the 1st- and 2nd-harmonic wave elevations at $(2r_d, 0)$ for the cylinder with $\theta = 80°$ in pitch motion at $kr_d = 2.0$. **a** 1st-harmonic; **b** 2nd-harmonic

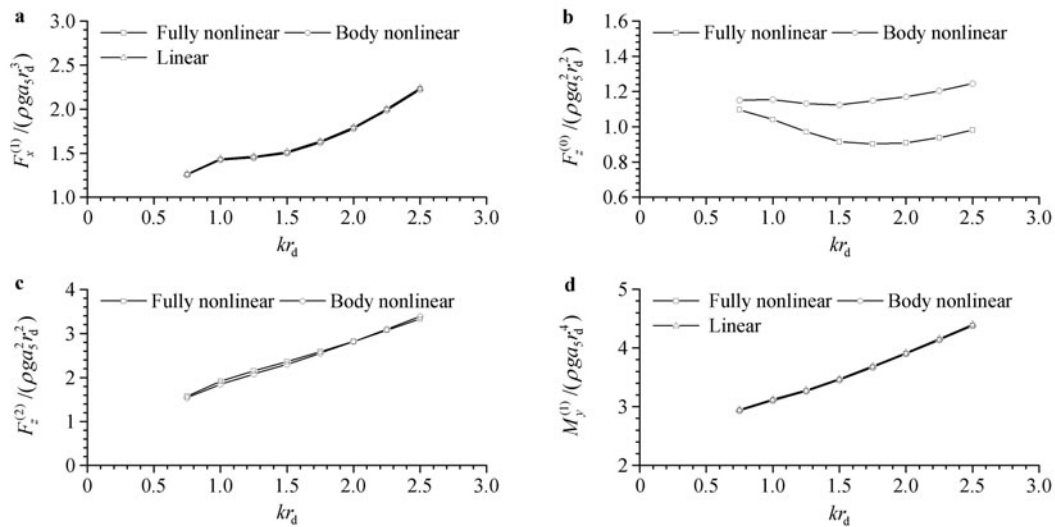**Fig. 21** Comparison of harmonic forces and moment on the cylinder with $\theta = 80°$ in pitch motion at $a_5 = \pi/30$. **a** 1st-harmonic horizontal force; **b** Mean vertical force; **c** 2nd-harmonic vertical force; **d** 1st-harmonic moment about the y-axis

constant at $a_5 = \pi/30$. As can see seen from Fig. 20a, the difference in the 1st-harmonic wave elevations becomes more significant with the increase in wave number. Moreover, the body-nonlinear results are closer to the linear solutions than the fully nonlinear results. However the difference in the 2nd-harmonic wave elevations is more prominent at lower-frequencies. The time histories of wave elevation at $(2r_d, 0)$ for $kr_d = 0.75$ and 2.5 are presented in Figs. 22a and 22b. It can be seen that there still exists difference between the fully nonlinear results and the body-nonlinear results both at $kr_d = 0.75$ and 2.5, in the wave crest for the former and the wave trough for the latter. As observed from Fig. 21b, the

difference in the mean vertical forces becomes more significant with increasing wave number, which also suggests that the nonlinearity of the vertical forces becomes stronger with the increase in the wave number. However, there is no noticeable difference among others. The discrepancy between the fully nonlinear results and the body-nonlinear solutions is mainly due to the variation of the instantaneous free surface, which is not considered in the body-nonlinear method. In the body-nonlinear model, the mean water surface is considered, while in the fully nonlinear models, the instantaneous surface is updated continuously.
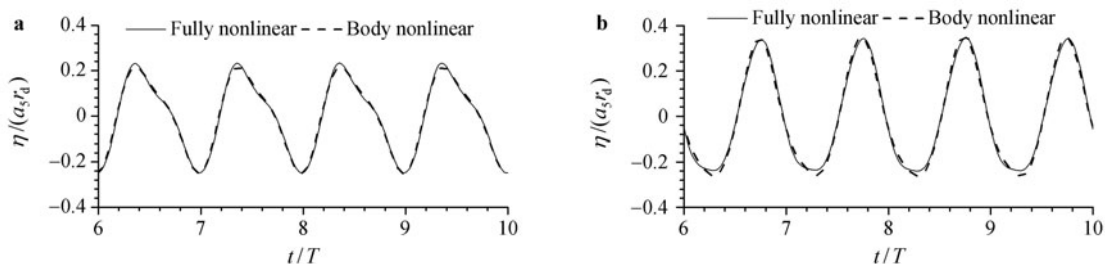

Fig. 22 Wave elevations at $(2r_d, 0)$ for the cylinder with $\theta = 80°$ in pitch motion at $a_5 = \pi/30$. **a** $kr_d = 0.75$; **b** $kr_d = 2.5$

5 Conclusions

A three-dimensional fully nonlinear numerical wave model is developed to simulate radiated waves generated by submerged or surface-piercing structures. subjected to forced sinusoidal motions. The model is solved in the time-domain by using the HOBEM. The body-nonlinear and linear models are also presented for comparison. For the purpose of validation, the present model is compared with the published numerical results, and reasonably good agreement between them is obtained. Wave radiation from a fully submerged sphere in heave motion and a truncated cylinder with flare undergoing forced heave and pitch motions is analyzed, and brief parametric study is performed to determine the effect of oscillation amplitude and frequency on wave elevations and hydrodynamic forces. The following observations can be concluded after a series of numerical calculations. For a surface-piercing structure in heave motion, the nonlinearity of the vertical force is very strong, even in the case where the generated waves are linear. For a truncated flared cylinder undergoing pitch motion, the vertical force oscillates at twice the frequency of the body motion. Its amplitude is smaller in comparison with that of the horizontal force, but it increases rapidly with the increase in the oscillation amplitude. Compared with the fully nonlinear method, the body-nonlinear method can also produce reasonable results for radiation problem if the wave frequency is low. Therefore, when the free-surface nonlinearity is not significant, the body-nonlinear method can be used as an alternative for the fully nonlinear scheme without the need to deal with complicated free surface and possible numerical instability. The difference between fully- and body-nonlinear results becomes significant at higher wave frequency, which reveals the limitation of the body-nonlinear method and the importance of the fully nonlinear method. The present model can be extended to simulate the interaction between surface waves and free floating bodies of arbitrary geometry.

References

1 Eatock Taylor, R., Hung, S.M.: Second order diffraction forces on a vertical cylinder in regular waves. Appl. Ocean Res. **9**, 19–30 (1987)

2 Abul-Azm, A.G., Williams, A.N.: Second-order diffraction loads on truncated cylinders. J. Waterway, Port, Coastal & Ocean Eng. **114**, 436–454 (1988)

3 Kim, Y., Kring, D.C., Sclavounos, P.D.: Linear and nonlinear interactions of surface waves with bodies by a three-dimensional Rankine panel method. Appl. Ocean Res. **19**, 235–249 (1997)

4 Bai, W., Teng, B.: Second-order wave diffraction around 3-D bodies by a time-domain method. China Ocean Eng. **15**, 73–85 (2001)

5 Goren, O.: On the second-order wave radiation of an oscillating vertical circular in finite-depth water. J. Ship Res. **40**, 224–234 (1996)

6 Isaacson, M., Ng, J.Y.T.: Second-order wave radiation of three-dimensional bodies by time-domain method. Int. J. Offshore Polar Eng. **3**, 264–272 (1993)

7 Teng, B., Bai, W., Dong, G.H.: Simulation of second-order radiation of 3D bodies in time domain by a B-spline method. In: Proc. of 12th International Offshore and Polar Engineering Conference, Kitakyushu, Japan, 487–493 (2002)

8 Wu, G.X.: Hydrodynamic forces on a submerged circular cylinder undergoing large-amplitude motion. J. Fluid Mech. **254**, 41–58 (1993)

9 Wu, G.X.: Hydrodynamic forces on a submerged sphere undergoing large amplitude motion. J. Ship Res. **38**, 272–277 (1994).

10 Zhu, D.X., Katory.: A time-domain prediction method of ship motions. Ocean Eng. **25**, 781–791 (1998)

11 Koo, W.C, Kim, M.H.: Numerical simulation of nonlinear wave and force generated by a wedge-shape wave maker. Ocean Eng. **33**, 983–1006 (2006)

12 Ferrant, P.: A coupled time and frequency approach for nonlinear radiation. In: Proc. of 18th Symposium on Naval Hydro, Ann Arbor, Michigan, 67–83 (1991)

13 Qiu, W., Peng, H.: Numerical solution of body-exact problem in the time domain with a panel-free method. In: Proc. of 22nd IWWWFB, Plitvice, Croatia (2007)

14 Longuet-Higgins, M.S., Cokelet, C.D.: The deformation of steep surface waves on water: I. A numerical method of computation. Proc. R Soc. Lond. A. **350**, 1–26 (1976)

15 Ma, Q.W., Wu, G.X., Eatock Taylor, R.: Finite element simulation of fully non-linear interaction between vertical cylinders and steep waves—Part 1: Methodology and numerical procedure. Int J. Numer. Meth. Fluids **36**, 265–285 (2001)

16 Ma, Q.W., Wu, G.X., Eatock Taylor, R.: Finite element simulation of fully non-linear interaction between vertical cylinders and steep waves—Part 2: Numerical results and validation. Int J. Numer. Meth. Fluids **36**, 287–308 (2001)

17 Hu, P.X., Wu, G.X., Ma, Q.W.: Numerical simulation of nonlinear wave radiation by a moving vertical cylinder. Ocean Eng. **29**, 1733–1750 (2002)

18 Wu, G.X., Hu, Z.Z.: Simulation of nonlinear interactions between waves and floating bodies through a finite-element-based numerical tank. Proc. R. Soc. Lond. A **460**, 2797–2817 (2004)

19 Wang, C.Z., Wu, G.X.: An unstructured mesh based finite element simulations of wave interactions with non-wall-sided bodies. J. Fluids Struct. **22**, 441–461 (2006)

20 Wang, C.Z., Wu, G.X., Drake, K.R.: Interactions between fully nonlinear water waves and non-wall-sided 3D structures. Ocean Eng. **34**, 1182–1196 (2007)

21 Xue, M., Xu, H., Liu, Y., et al.: Computations of fully nonlinear three dimensional wave–wave and wave–body interactions. Part 1. Dynamics of steep three-dimensional waves. J. Fluid Mech. **438**, 11–39 (2001)

22 Xue, M., Xu, H., Liu, Y., et al.: Computations of fully nonlinear three dimensional wave–wave and wave–body interactions. Part 2. Nonlinear waves and forces on a body. J. Fluid Mech. **438**, 41–46 (2001)

23 Bai, W., Eatock Taylor, R.: Higher-order boundary element simulation of fully nonlinear wave radiation by oscillating ver-

tical cylinders. Appl. Ocean Res. **28**, 247–265 (2006)

24 Bai, W., Eatock Taylor, R.: Numerical simulation of fully nonlinear regular and focused wave diffraction around a vertical cylinder using domain decomposition. Appl. Ocean Res. **29**, 55–71 (2007)

25 Bai, W., Eatock Taylor, R.: Fully nonlinear simulation of wave interaction with fixed and floating flaRes. structures. Ocean Eng. **36**, 223–236 (2009).

26 Bai, W., Feng, X., Eatick Taylor, R., et al.: Fully nonlinear analysis of near-trapping phenomenon around an array of cylinders. Appl. Ocean Res. **44**, 71–81 (2014)

27 Ning, D.Z., Zhou, B.Z., Teng, B., et al.: Numerical simulation of nonlinear regular and focused waves generated by a piston wave maker. In: Proc. of the 5th international conference on Asian and Pacific Coasts, Singapore (2009)

28 Zhou, B.Z., Teng. B, Ning, D.Z., et al.: Fully Nonlinear Wave Diffraction by a velocity potential division method. In: Proc. of the 22nd International Offshore and Polar Engineering Conference, Rhodes, Greece (2012)

29 Liu, Y.Z., Miao, G.P.: Theory of Ship Motions in Waves. Shanghai Jiao Tong University Press, Shanghai (1987) (in Chinese)

30 Ning, D.Z., Zhou, B.Z., Teng, B.: Numerical simulation of nonlinear wave generation by a piston wave maker in a step-type wave flume. Advances in Eng. Res. **2** (2011)

31 Wu, G.X.: Transient motion of a floating body in steep water waves. In: Proc. of 11th IWWWFB, Hamburg, Germany (1996)

32 Wu, G.X., Eatock Taylor, R.: The coupled finite element and boundary element analysis of nonlinear interactions between waves and bodies. Ocean Eng. **30**, 387–400 (2003)

33 Kashiwagi, M.: Non-linear simulations of wave-induced motions of a floating body by means of the mixed Eulerian-Lagrangian method. In: Proc. Inst. Mech. Engrs. C, **214**, 841–855 (2000)

34 Grilli, S.T., Guyenne, P., Dias, F.A.: Fully non-linear model for three-dimensional overturning waves over an arbitrary bottom. Int. J. Numer. Meth. Fluids **35**, 829–867 (2001)